

Electrocaloric refrigeration: From physical fundamentals to practical devices

Feiyu Zhang(张费宇), Tiannan Yang(杨天南), and Xiaoshi Qian(钱小石)
Citation: Chin. Phys. B, 2026, 35 (**2**): 027701. DOI: 10.1088/1674-1056/ae1f80
http://cpb.iphy.ac.cn; http://iopscience.iop.org/cpb

What follows is a list of articles you may be interested in

Positive and negative electrocaloric effects

Hongrui Xu(徐洪瑞) and Jiping Huang(黄吉平)
Chin. Phys. B, 2025, 34 (**6**): 067702. DOI: 10.1088/1674-1056/adc36c

Understanding thermal hysteresis of ferroelectric phase transitions in $BaTiO_3$ with combined first-principle-based approach and phase-field model

Cancan Shao(邵灿灿) and Houbing Huang(黄厚兵)
Chin. Phys. B, 2025, 34 (**2**): 027701. DOI: 10.1088/1674-1056/ad9e94

Electrocaloric effect enhanced thermal conduction of a multilayer ceramic structure

Hongbo Liu(刘宏波)
Chin. Phys. B, 2020, 29 (**8**): 087701. DOI: 10.1088/1674-1056/ab942f

Electrocaloric effect and pyroelectric properties of organic-inorganic hybrid $(C_2H_5NH_3)_2CuCl_4$

Yi Liu(刘义), Yan-Fen Chang(畅艳芬), Young Sun(孙阳), Jun Shen(沈俊), Li-Qin Yan(闫丽琴), Zun-Ming Lu(卢遵铭)
Chin. Phys. B, 2019, 28 (**11**): 117701. DOI: 10.1088/1674-1056/ab48db

Effect of an electric field on the electrocaloric response of ferroelectrics

Hongbo Liu(刘宏波)
Chin. Phys. B, 2018, 27 (**12**): 127701. DOI: 10.1088/1674-1056/27/12/127701

TOPICAL REVIEW — Multiferroicity and multicaloric effects

Electrocaloric refrigeration: From physical fundamentals to practical devices

Feiyu Zhang(张费宇), Tiannan Yang(杨天南)[‡], and Xiaoshi Qian(钱小石)[†]

State Key Laboratory of Mechanical System and Vibration, Interdisciplinary Research Center, Institute of Refrigeration and Cryogenics, and MOE Key Laboratory for Power Machinery and Engineering, School of Mechanical Engineering, Shanghai Jiao Tong University, Shanghai 200240, *China*

(Received 28 September 2025; revised manuscript received 10 November 2025; accepted manuscript online 14 November 2025)

The electrocaloric (EC) effect refers to the change in the polarization entropy and/or temperature of dielectric materials when an electric field is applied and removed. EC refrigeration has received increasing interest as an alternative to conventional refrigeration technologies because it provides both high energy efficiency and zero global warming potential. In this review, we first introduce the thermodynamic fundamentals of the EC effect and the mechanism of EC refrigeration cycles. We then present recent advances in EC cooling technologies, from material improvements to device demonstrations, including a critical analysis of existing material and device characterization methodologies and a discussion of how to reliably measure the parameters of materials and devices. Finally, the current challenges and possible future prospects for EC cooling technology are outlined.

Keywords: electrocaloric effect, refrigeration, electrocaloric cooling devices, electrocaloric materials

PACS: 77.70.+a, 77.84.–s, 85.50.–n, 07.20.–n

DOI: 10.1088/1674-1056/ae1f80 **CSTR:** 32038.14.CPB.ae1f80

1. Introduction

With the intensification of global climate change and the continuous increase in energy consumption, the limitations of traditional refrigeration technologies, such as vapor-compression systems, have become increasingly prominent. These traditional technologies typically rely on refrigerants with high global warming potential (GWP), such as hydrofluorocarbons (HFCs), which exacerbate the greenhouse effect; in addition, these technologies suffer from low energy efficiency, high noise levels, and bulky designs. As a result, the development of sustainable and energy-efficient cooling technologies that minimize environmental impact is urgently needed.

To address these challenges, various green refrigeration technologies, including thermoelectric (TE),[1] magnetocaloric effect (MCE),[2–4] elastocaloric/barocaloric effect (eCE/BCE),[5,6] and electrocaloric effect (ECE)[7,8] cooling, have emerged. Among these options, thermoelectric cooling has already been commercialized, but its low energy efficiency limits its large-scale application. In contrast, caloric refrigeration technologies that are driven by external fields (magnetic, stress, or electric fields) demonstrate higher energy efficiency potential.[9] In particular, the electrocaloric (EC) effect has gained attention because of its high theoretical efficiency, fast response, compact design, and zero greenhouse gas emissions.[10]

The ECE refers to the change in polarization entropy and/or temperature in dielectric materials when an electric field is applied and removed. The ECE was first theorized in the 1930s[11] but remained largely unexplored until advances in material science enabled the discovery of giant ECE in ferroelectric ceramics[7] and polymers[8] in the early 2000s. Recent breakthroughs in material engineering and device fabrication have further positioned EC refrigeration as a viable next-generation refrigeration technology for applications that range from microelectronics to domestic appliances.[12]

This paper is organized as follows. Section 2 presents the fundamental theory of the ECE, analyzes the limitations of current measurement methods, and introduces an *in-situ* calibrated measurement approach. Furthermore, the phase-field theory, negative ECE, and anomalous ECE are discussed in this section to provide a comprehensive understanding of various EC-related phenomena. Section 3 reviews recent breakthroughs in EC materials, with a particular emphasis on performance comparison, while highlighting the emerging high-entropy strategy. Section 4 discusses the thermodynamic cycles of EC refrigeration systems and their corresponding key parameters. Section 5 explores the design and optimization of EC devices and highlights prototype demonstrations and their cooling capabilities. Finally, the summary section discusses challenges and future directions for EC technology.

[†]Corresponding author. E-mail: xsqian@sjtu.edu.cn

[‡]Corresponding author. E-mail: yangt@sjtu.edu.cn

© 2026 Chinese Physical Society and IOP Publishing Ltd. All rights, including for text and data mining, AI training, and similar technologies, are reserved.

2. Fundamentals of the electrocaloric effect

2.1. Thermodynamics and phenomenological theory of the ECE

The ECE originates from the coupling between electric and thermal fields in dielectric materials under an applied electric field. From a thermodynamic perspective, the ECE arises because of the field-induced change in entropy, which leads to reversible heating or cooling. Its basic principle is shown in Fig. 1.



Fig. 1. Schematic illustration of the ECE. The arrows represent electrical dipoles.

In general, the Gibbs free energy G for a dielectric material can be expressed as a function of the temperature T, entropy S, stress X, strain x, electric field E and electric displacement D as follows:

$$G = U - TS - X_i x_i - E_j D_j, \tag{1}$$

where U denotes the internal energy of the EC system and the stress and field terms are written in Einstein notation, where i ranges from 1 to 6 and j ranges from 1 to 3. The differential form of Eq. (1) is

$$\mathrm{d}G = -S\mathrm{d}T - x_i \mathrm{d}X_i - D_j \mathrm{d}E_j. \tag{2}$$

The entropy S, strain x, and electric displacement D_j are expressed as follows:

$$\begin{aligned} S &= -\left(\frac{\partial G}{\partial T}\right)_{X,E}, \quad x_i = -\left(\frac{\partial G}{\partial X_i}\right)_{T,E}, \\ D_j &= -\left(\frac{\partial G}{\partial E_j}\right)_{T,X}. \end{aligned} \tag{3}$$

Equation (3) leads to the following Maxwell relation:

$$\left(\frac{\partial S}{\partial E_j}\right)_{T,X} = \left(\frac{\partial D_j}{\partial T}\right)_{X,E}. \tag{4}$$

For a reversible thermodynamic process, with no pressure or volume work in the EC system, the equation for the specific internal energy u of the system can be simplified to

$$u = T\mathrm{d}S + E\mathrm{d}P. \tag{5}$$

In EC materials, the entropy S at given electric field E and temperature T can be divided as follows:

$$S(E,T) = S_{\mathrm{dip}}(E,T) + S_{\mathrm{N-dip}}(T), \tag{6}$$

where S_{dip} is associated with the dipolar entropy (the polarization state of the insulators) and $S_{\mathrm{N-dip}}$ represents the entropies that, despite their strong dependence on temperature, are independent of the electric field, such as the lattice entropy and the electron entropy.[13] The isothermal entropy change ΔS solely associated with dipolar entropy when the electrical field E changes from E_1 to E_2 ($\Delta E = E_2 - E_1$) at temperature T can be expressed as follows:

$$\Delta S_{\mathrm{EC}}(E,T) = S_{\mathrm{dip}}(E_2,T) - S_{\mathrm{dip}}(E_1,T) = S_{\mathrm{dip}}(E,T). \tag{7}$$

Under adiabatic condition ($\Delta S = 0$), there will be a temperature change $\Delta T = T_2 - T_1$. The following relation can be obtained:

$$S_{\mathrm{dip}}(E_2,T_2) - S_{\mathrm{dip}}(E_1,T_1) = -(S_{\mathrm{N-dip}}(T_2) - S_{\mathrm{N-dip}}(T_1)). \tag{8}$$

The $\Delta S_{\mathrm{N-dip}}$ cannot be directly measured but can be calculated from the heat capacity at zero electric field. The heat capacity is defined as

$$c_E = T\left(\frac{\partial S}{\partial T}\right)_E. \tag{9}$$

Under zero electric field, ferroelectric materials are typically in the paraelectric phase or in a state where the polarization is random and disordered. In this state, the sensitivity of the dipole system to temperature $(\partial S_{\mathrm{dip}}/\partial T)_E$ is very small and can even be considered negligible. Therefore, under zero electric field, the non-dipolar entropy change induced by a temperature change ΔT is given by

$$\Delta S_{\mathrm{N-dip}}(T) = \int_{T_1}^{T_2} \frac{c_0 T}{T}\mathrm{d}T. \tag{10}$$

Based on Eq. (10), the contribution of non-dipolar entropy can be separated. The dominant contribution of S_{dip} or $S_{\mathrm{N-dip}}$ is highly material- and temperature-dependent. In ferroelectric materials exhibiting a sharp first-order phase transition, the ECE is often dominated by the configurational entropy change of the dipoles, as the electric field can induce a large-scale reorientation of polar domains or even a phase transition. Conversely, in relaxor ferroelectrics or in regimes away from the phase transition, the contribution from the lattice entropy can become comparable or even dominant.

The total differential of the total entropy is defined as follows:

$$\mathrm{d}S(E,T) = \left(\frac{\partial S}{\partial T}\right)_E \mathrm{d}T + \left(\frac{\partial S}{\partial E}\right)_T \mathrm{d}E. \tag{11}$$

The heat exchange can be expressed as follows:

$$\delta Q(E,T) = T\mathrm{d}S = T\left(\frac{\partial S}{\partial T}\right)_E \mathrm{d}T + T\left(\frac{\partial S}{\partial E}\right)_T \mathrm{d}E. \tag{12}$$

By relating Eqs. (4) and (9) the following relation can be obtained:

$$-\left(\frac{\partial T}{\partial E_j}\right)_S = \frac{T}{c_E}\left(\frac{\partial D}{\partial T}\right)_E, \tag{13}$$

where c_E represents the heat capacity. Under a constant stress X, the isothermal entropy change ΔS and adiabatic temperature change ΔT of an ECE material as the electric field E changes from E_1 to E_2 can be expressed as follows:

$$\Delta S = \int_{E_1}^{E_2} \left(\frac{\partial D}{\partial T}\right)_{E,X} \mathrm{d}E, \tag{14}$$

$$\Delta T = -\int_{E_1}^{E_2} \frac{T(E)}{c_E(T)} \left(\frac{\partial D}{\partial T}\right)_{E,X} \mathrm{d}E. \tag{15}$$

While Maxwell's relations provide a universal thermodynamic framework for the ECE, they do not explicitly account for the microscopic mechanisms or phase transitions that govern the polarization response in ferroelectric and relaxor materials. To bridge this gap, we now turn to Landau–Devonshire (L-D) phenomenological theory, which describes polarization behavior through free energy expansion.

The L-D phenomenological theory has been widely used to describe the macroscopic phenomena that occur in polar materials near their phase transitions. According to the L-D theory, the Gibbs free energy of a ferroelectric material can be written as an expansion of the polarization P (for most ferroelectrics, $P \approx D$) as follows:

$$G = G_0 + \frac{1}{2}\alpha P^2 + \frac{1}{4}\xi P^4 + \frac{1}{6}\zeta P^6 + \cdots - EP. \tag{16}$$

In general, the coefficient α is temperature-dependent and ξ, ζ, ... are temperature independent. In ferroelectrics, $\alpha(T) = \beta(T - T_0)$, where β represents a material-dependent constant, and T_0 represents the instability temperature.

According to the L–D phenomenological theory,

$$\Delta S = -\frac{1}{2}\beta\left[P^2(E_\mathrm{H}) - P^2(E_\mathrm{L})\right] = -\frac{1}{2}\beta P^2, \tag{17}$$

where $E_\mathrm{L} = 0$ and $\beta = \ln(\Omega)/(\varepsilon_0\Theta)$.[14] Here E_L represents the low electric field, E_H denotes the high electric field, ε_0 denotes the permittivity of vacuum, and Θ denotes an effective Curie constant, which is directly related to the polar correlation in dielectrics. Thus, a large Ω, which corresponds to the number of polar entities that are accessible by dipoles, and a weak polar correlation Θ result in a large β value and a giant ECE at low fields.[15]

By relating Eqs. (13) and (17) the adiabatic temperature change under an electric field can be obtained as follows:

$$\Delta T_\mathrm{EC} = \frac{1}{2c_E}\beta T P^2. \tag{18}$$

The preceding derivation omits explicit consideration of secondary pyroelectric effects, which are present in numerous EC materials. For a more thorough theoretical treatment of this aspect, readers may refer to the comprehensive review articles by Rožič *et al.*[16] and Li *et al.*[17]

2.2. ECE measurement

The ECE stems from electric-field-induced changes in dipolar ordering. Since direct measurement of dipolar ordering remains experimentally challenging, for ECE characterization, two principal approaches are typically employed: (1) polarization-based analysis (indirect method) and (2) thermally derived analysis (direct method). The designation of "directness" primarily reflects how thermal (heat flux or temperature) measurements are more immediately correlated with the primary application of active heat pumping than polarization measurements, which are used to assess dielectric properties.

Most of the indirect measurements are based on results that are derived from Maxwell's relation, which is expressed in Eq. (4), from which the isothermal entropy change ΔS and adiabatic temperature change ΔT of the ECE as the electric field changes from E_1 to E_2 can be deduced, as expressed in Eqs. (14) and (15). The indirect method has been extensively employed for ECE characterization since the 1960s,[18] primarily because polarization measurement systems, which track polarization versus temperature, are experimentally convenient. For a thermodynamically reversible system, Maxwell's relation conveniently connects the dielectric parameters to the thermal parameters. However, a fundamental limitation arises because Maxwell's relations are valid only for ergodic systems. This imposes significant constraints on the use of polarization-based indirect methods to characterize the ECE in materials such as relaxor ferroelectric polymers, where the domain dynamics exhibit inherent irreversibility.[19]

Direct measurement of the ECE involves the characterization of the temperature change or heat flow in materials upon application or removal of electric fields, which provides the most straightforward experimental evidence. Changes in the temperature of in EC materials can be directly monitored via either contact or noncontact methods. Thermocouple measurements provide point-specific data when the sensor is affixed to the sample surface center to record transient thermal responses to applied electric fields.[19,20] For comprehensive spatial analysis, infrared cameras offer noninvasive mapping of surface temperature distributions, thereby facilitating high-resolution monitoring of thermal dynamics at ultrashort timescales.[21] At the microscale, scanning thermal microscopy (SThM) techniques enable nanoscale ECE characterization via the use of a thermally sensitive atomic force microscopy (AFM) probe that detects localized temperature changes that are induced by an applied electric field.[22,23] Differential scanning calorimetry (DSC) is the most common thermal technique for heat flow measurement, where controlled electric fields are applied to a sample while the heat flow is precisely monitored.[24,25] This technique results in the detection of distinct exothermic and endothermic peaks that directly correlate with the application and re-

moval of the electric field.[26] Alternatively, researchers employ thermistor-based detection or specialized heat flux sensors to quantify the thermal response of ECE materials,[19,27] with advanced configurations incorporating reference resistor heaters for improved measurement accuracy through *in-situ* calibration.[28–31]

The accuracy of the direct method depends on the conditions during measurement being near-adiabatic; otherwise, the results of the direct method will be underestimated. When an electric field is applied (Fig. 2(a)), the temperature instantaneously increases and remains stable but then immediately returns to its baseline level upon field removal (Fig. 2(b)) under ideal adiabatic conditions. However, the nonnegligible heat capacities of both EC materials and heat flux sensors introduce thermal inertia, which results in gradual thermal transients (sloped edges rather than sharp steps). Thermal equilibration between the film and substrate occurs rapidly and is difficult to avoid. Consequently, the temperature change induced by the ECE will quickly equilibrate with the substrate, which makes accurate detection of the temperature change difficult.[32] Limited electric field slew rates and polarization relaxation kinetics delay changes in polarization, which causes thermal hysteresis in the temperature profile as well (Fig. 2(c)). The actual nonadiabatic response includes both thermal hysteresis and heat exchange with the surroundings. For example, when the EC material is placed in a low-conductivity medium such as air, the heat flux changes more slowly (Fig. 2(d)), whereas on a highly thermally conductive substrate, the heat flux changes faster (Fig. 2(e)). Most direct measurements of the ECE yield measurable temperature values (ΔT_{meas}) that deviate from the ideal adiabatic temperature response (ΔT_{adia}). From this perspective, the accuracy of ECE measurements cannot be guaranteed or compared across different operating conditions or when different types of sensors are used.

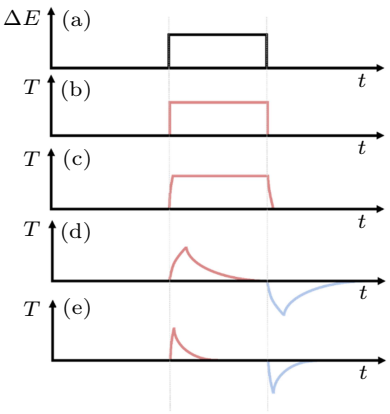


Fig. 2. Schematic illustration of the temperature–time profiles of an EC material under an applied electric field: (a) input electric field, (b) ideal adiabatic temperature response, (c) adiabatic response with a delay that is caused by heat exchange, (d) actual measurable response with a delay and slow heat exchange, and (e) actual measurable response with a delay and fast heat exchange.

The above methods face limitations in terms of either thermal isolation control or signal delay. Hence, an *in-situ* calibrated heat flow measurement approach was developed to address these challenges. By synchronizing electric field modulation with real-time thermal compensation, this method enables direct extraction of adiabatic temperature changes (ΔT_{ad}) while inherently correcting thermal leakage effects. The heat that is absorbed/ejected by the EC material when the electric field is removed/applied is measured via an *in-situ* calibrating calorimeter. The heat signal is recorded by a heat flux sensor. The recorded data are calibrated by using the reference heat that is produced by metal electrodes that are coated on the surface of the EC film. As shown in Fig. 3(a), after the electrodes on the top and bottom sides of the EC film are sputtered, two wires are connected to the bottom electrode and one wire is connected to the top electrode. The bottom electrode/reference heater generates a small amount of Joule heat (Q_{Joule}) when a pulse voltage (U) is applied (Fig. 3(b)) through the bottom via the two wires that are connected to it. The heat that is conducted to the heat flux sensor is captured and displayed as a voltage change (V_{Joule}). The EC material also generates heat (Q_{ECE}) when a high voltage is applied/removed (Fig. 3(c)) across the top and bottom electrodes. The rationale behind our design of this testing device is twofold. Firstly, it isolates the high-voltage terminal from the heat flow sensor, thereby protecting the sensor's longevity. Secondly, since the lower surface of the film is in direct contact with the heat flow sensor, we ensure that both the reference heat and the electrocaloric heat are directly received by the heat flow sensor. Under the same thermal boundary conditions as the reference heater measurement, the EC-induced heat signal is captured by the heat flux sensor and displayed as a voltage change (V_{ECE}). The reference Joule heat can be calculated according to Joule's law

$$Q_{\mathrm{Joule}} = \int \frac{U^2}{R}\,\mathrm{d}t. \tag{19}$$

The total heat that is generated by the ECE is calculated by the following equation:

$$Q_{\mathrm{ECE}} = Q_{\mathrm{Joule}} \frac{\int V_{\mathrm{ECE}}\,\mathrm{d}t}{\int V_{\mathrm{Joule}}\,\mathrm{d}t}. \tag{20}$$

The change in isothermal entropy is calculated by the following equation:

$$\Delta S = \frac{Q_{\mathrm{ECE}}}{T}, \tag{21}$$

where T denotes the room temperature. The temperature change in the EC material is calculated by the following equation:

$$\Delta T = \frac{Q_{\mathrm{ECE}}}{\rho V C_p} = \frac{Q_{\mathrm{ECE}}}{\rho \pi r^2 d C_p}, \tag{22}$$

where ρ denotes the density of the EC material, C_p represents the specific heat capacity, r denotes the radius of the overlap area of the electrodes, and d denotes the thickness of the EC film.

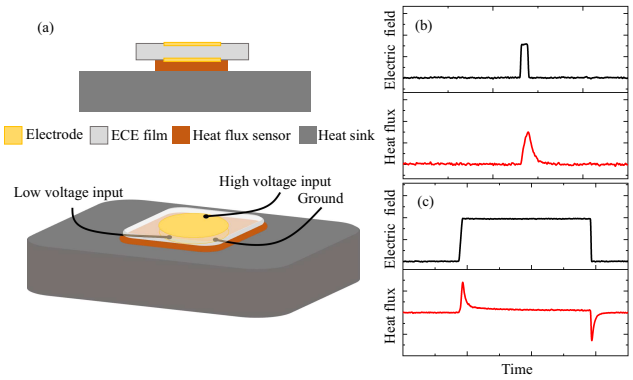


Fig. 3. (a) Schematic illustration of the *in-situ* calibrating ECE measurement device. (b) Waveforms of the applied electric field and heat flow signal during reference heat measurement, and (c) waveforms of the applied electric field and heat flow signal during ECE measurement.

2.3. Phase-field theory for the ECE

The ECE refers to the change in the polarization entropy and/or temperature of a dielectric material, which can be theoretically described by phase-field modeling. This approach provides a powerful framework for simulating the evolution of microstructures, domain dynamics, and the resulting EC properties in both inorganic and organic materials. Phase-field models incorporate thermodynamic free energy functionals, kinetic equations, and electrostatic interactions to capture the coupled effects of electric, elastic, and thermal fields.

The main principle of phase-field simulations lies in the use of a set of spatially continuous state variables to characterize the structural state within a material. These state variables are typically referred to as order parameters. They can describe complex microstructural features such as phase distributions, grain structures, and polarization domains. At any spatial point within the material system, the order parameters can vary continuously, and their values reflect the specific phase or structural state at that location. In ferroelectric materials, the order parameter is typically the ferroelectric polarization field $P(x)$, where x represents the spatial position vector. The stable state of the system under given external conditions is simulated by evolving the polarization field to equilibria as governed by the time-dependent Ginzburg–Landau equation, which can be expressed as follows:

$$\frac{\partial P}{\partial t} = L\left(-\frac{\partial F_P}{\partial P} + E^{\text{therm}}\right). \tag{23}$$

Equation (23) describes a relaxation process of the system that is driven by a minimization of the free energy of the system under given conditions, where t represents time; L represents a kinetic coefficient that reflects the sensitivity of the system's response to the driving force of free energy; F_P represents the polarization-dependent part of the free energy formulated as a function of the polarization field P and external conditions, including the external electric field E^{ext} and temperature T; and E^{therm} represents a random field that arises from thermal fluctuations, and obeys a normal distribution with the strength given by the fluctuation–dissipation theorem.[33]

Following existing phase-field theories,[34] the free energy F_P is equal to the sum of the Landau free energy, the gradient energy, the electrostatic energy, and the elastic energy, i.e.,

$$F_P = F_{\text{Landau}} + F_{\text{gradient}} + F_{\text{electrostatic}} + F_{\text{elastic}}. \tag{24}$$

The Landau free energy holds significant physical importance in phase-field models. It reveals the thermodynamic stability and evolution trends of a system under different polarization states and serves as the core thermodynamic foundation for describing material phase transitions, polarization behavior, and structural formation. The energy contributions are expressed as follows:

$$F_{\text{Landau}} = \int \left(a_{ij}P_iP_j + a_{ijkl}P_iP_jP_kP_l + a_{ijklmn}P_iP_jP_kP_lP_mP_n\right)\mathrm{d}x^3, \tag{25}$$

where indices i, j, k, and $l = 1,2,3$ indicate components of a vector or a tensor in Cartesian coordinates. An Einstein summation convention over repeated indices i, j, k and l is employed. a_{ij}, a_{ijkl}, and a_{ijklmn} represent the second-, fourth-, and sixth-order Landau coefficients, respectively. In particular, the diagonal components of the second-order coefficient a_{ij} are typically temperature-dependent according to the Curie–Weiss law, i.e., $a_{ii}(T) \propto (T - T_{\text{CW}})$, where T_{CW} represents the Curie–Weiss temperature. The temperature dependence of the free energy functional inherently accounts for the coupling between the polarization and the thermal functions of the system, including the ECE.

The gradient energy in phase-field models represents the energy cost that is required to maintain the spatial continuity of the polarization field. It characterizes the energy that is necessary for the transition from ferroelectric to paraelectric phases. The gradient energy can be expressed as follows:

$$F_{\text{gradient}} = \int g_{ijkl}\frac{\partial P_i}{\partial x_j}\frac{\partial P_k}{\partial x_l}\mathrm{d}x^3, \tag{26}$$

where g represents the gradient energy coefficient.

The electrostatic energy is a component that describes the interaction between the polarization and electric fields within a ferroelectric material. It reflects the coupling relationship between the polarization field and the electric field. It is typically expressed as

$$F_{\text{electrostatic}} = \int \left(-\frac{1}{2}E_i^{\text{d}}P_i - E_i^{\text{ext}}P_i\right)\mathrm{d}x^3, \tag{27}$$

where $E^{\text{d}}(x)$ represents the depolarization field that is obtained by solving the electrostatic equilibrium equation at every evolution time step.

The elastic energy describes the energy variation in a material that results from mechanical deformation, including spontaneous strain, applied stress, and thermal expansion. The elastic energy is expressed as follows:

$$F_{\text{elastic}} = \int \frac{1}{2}c_{ijkl}\left(\varepsilon_{ij} - \varepsilon_{ij}^0\right)\left(\varepsilon_{kl} - \varepsilon_{kl}^0\right)\mathrm{d}x^3, \tag{28}$$

where c represents the elastic stiffness tensor, ε represents the strain field that is obtained by solving the mechanical equilibrium equation, and ε^0 represents the eigenstrain field, which is given by $\varepsilon^0_{ij} = Q_{ijkl}P_kP_l$, with Q being the electrostrictive coefficient. A combination of Eqs. (23)–(28) yields the spatiotemporal microstructural response of the modeled material system to given external conditions.

The EC entropy change is further calculated on the basis of simulated polarization response to external electric fields. Following the fundamental equation of the total free energy F_{total},

$$S = -\left(\frac{\partial F_{\text{total}}}{\partial T}\right)_{E^{\text{ext}}}. \tag{29}$$

The free energy is separated into two parts, namely, a polarization-dependent component F_P, which represents the contribution of the polar order and depends on both the temperature and the external field, and the remaining component F_0, which is independent of the external field:

$$F_{\text{total}} = F_P\left(E^{\text{ext}},T\right) + F_0\left(T\right). \tag{30}$$

Notably, F_P is given by Eq. (24) of the phase-field model, where the simulated equilibrium-state polarization distribution $P(x)$ of a given condition (E^{ext},T) is considered. For an isothermal process at a constant temperature, the EC entropy change is given by

$$\begin{aligned}\Delta S_{E_{\text{a}}^{\text{ext}}\to E_{\text{b}}^{\text{ext}}} &= S\left(E_{\text{b}}^{\text{ext}},T\right) - S\left(E_{\text{a}}^{\text{ext}},T\right)\\ &= -\left(\left.\frac{\partial F_P}{\partial T}\right|_{E^{\text{ext}}=E_{\text{b}}^{\text{ext}}} - \left.\frac{\partial F_P}{\partial T}\right|_{E^{\text{ext}}=E_{\text{a}}^{\text{ext}}}\right),\end{aligned} \tag{31}$$

upon varying the external field from $E_{\text{a}}^{\text{ext}}$ to $E_{\text{b}}^{\text{ext}}$. The function $F_0(T)$ is therefore not needed for calculating the EC entropy change. The derivatives with respect to the temperature T in Eq. (31) are then evaluated by simulating two system states under slightly different temperatures:

$$\frac{\partial F_P}{\partial T} \approx -\frac{F_P(T+\delta T) - F_P(T)}{\delta T}. \tag{32}$$

It is important to note that while phase-field modeling provides profound insights, its predictions may exhibit deviations from experimental measurements, similar to the indirect measurement methods discussed earlier. These deviations primarily stem from several idealized assumptions inherent in the model. First, the accuracy of simulations is contingent on the input parameters (e.g., Landau coefficients, gradient energy coefficients), which are often derived from limited experimental data or first-principles calculations, and their simplified temperature dependence may not fully capture complex material behavior across a broad temperature range. Second, phase-field models operate on mesoscopic spatial and temporal scales that are typically more limited than experimental conditions, which can affect the prediction of long-range domain dynamics and complete relaxation processes. Finally, while the model calculates the intrinsic ECE under idealized adiabatic or isothermal conditions within the simulation box, practical measurements are susceptible to thermal losses and limited heat transfer within the sample and to sensors, often resulting in a lower measured temperature change than the theoretically predicted adiabatic value.

In phase-field models, by coupling the evolution of the polarization order parameter with the thermodynamic potential and microstructural state of the system, not only quantitatively analyzing the entropy change behavior between different polarized states but also revealing the specific influence mechanisms of material structures, such as crystallinity and defect distribution, on the EC response are possible.

2.4. Negative ECE

The negative electrocaloric effect (NECE), which is also known as the inverse ECE, is a unique phenomenon that differs from the conventional ECE. In the NECE, applying an external electric field lowers the material temperature, while removing the field increases it. The ECE in antiferroelectrics had not received much attention until the discovery of the NECE in 2011.[35] The NECE has since been widely reported in various material systems, including antiferroelectric materials,[36] point-defect-engineered ferroelectric materials,[37,38] and multilayer ferroelectric thin films,[39] among others. Interestingly, both the ECE and the NECE can coexist in the same material or appear separately in different systems. Among the different types of NECE materials, antiferroelectric systems, which are represented by $PbZrO_3$, have attracted particularly significant research interest. Researchers have reported that combining the ECE and NECE can significantly enhance solid-state cooling performance, thus offering promising potential for advanced EC refrigeration.[40–42]

The underlying microscopic mechanism of the NECE remains uncertain, although several theoretical models have been developed to explain this phenomenon. Among these, the dipole canting model provides a compelling explanation.[36] In the absence of an external electric field, the dipoles in antiferroelectric materials arrange themselves in an ordered antiparallel alignment, which corresponds to a low polarization entropy state (Fig. 4(a)).[43] Antiferroelectric materials exhibit ordered dipole alignment in both their antiferroelectric and ferroelectric phases, both of which correspond to a low polarization entropy state. When a moderate electric field is applied, the electric dipoles undergo a characteristic cone-like precession along the field direction and the radius of the $P+$ cone decreases whereas the radius of the $P-$ cone increases. (Fig. 4(b)). This dynamic behavior causes significant fluctuations in the polarization components perpendicular to the applied field, whereas the longitudinal component (parallel to

the field) remains relatively stable. The increased disorder in the transverse polarization orientation increases the dipolar entropy, which consequently produces the observed temperature decrease characteristic of the NECE. The electric-field-induced increase in polarization entropy occurs exclusively during the antiferroelectric-to-ferroelectric phase transition. When the electric field is strong enough, the dipoles tend to align with the electric field, and the system returns to the positive EC effect. This theory is also applicable to some aforementioned material systems that exhibit NECEs.[44]

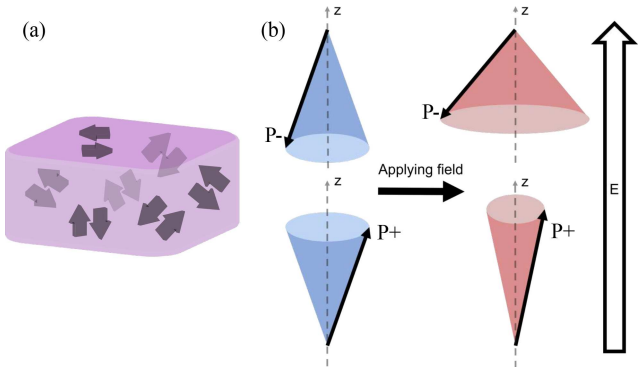


Fig. 4. (a) Electric domain of antiferroelectrics before being polarized and (b) the transition of the parallel and antiparallel dipoles from the zero-field state to the field-applied state.

Other hypotheses, including defect-dipole-induced mechanisms[37] and the contribution of latent heat,[44] have been proposed to explain the NECE. A promising strategy for inducing the NECE involves the application of a subcoercive negative electric field ($E \ll E_C$) to a positively poled ferroelectric material. This weak negative field partially disrupts the well-aligned dipole configuration, thereby generating a controlled entropy increase. Owing to strong interdomain coupling in bulk ferroelectrics, when the applied field energy remains below the double-well potential barrier, the system spontaneously recovers its original polarization orientation upon field removal.[45] This reversible process creates a small but measurable NECE.

Unlike the ECE and NECE which produce balanced heating-cooling signal pairs during full electric field cycles, the anomalous electrocaloric effect (AECE) exhibits a cooling-only response under complete field cycling (Fig. 5). The exclusive cooling signature of the AECE, which is devoid of any heating component within a cycle, represents a unique phenomenon. Here, a precise equilibrium between ordered (FE) and disordered (relaxor) domains enables this behavior.[45] When a negative field pulse near the coercive field is applied, the polarization decreases to zero without switching, which triggers an increase in entropy and sustained cooling. Because of the unique cooling-only effect, the AECE may be used for cooling-power storage.

While emerging EC phenomena such as the NECE and AECE continue to attract research interest, the positive ECE remains the most technologically viable mechanism for solid-state refrigeration applications because of its superior cooling performance. Recent advances have demonstrated giant ECE responses in various material systems, which have achieved remarkable cooling capacities that approach practical requirements for thermal management devices.

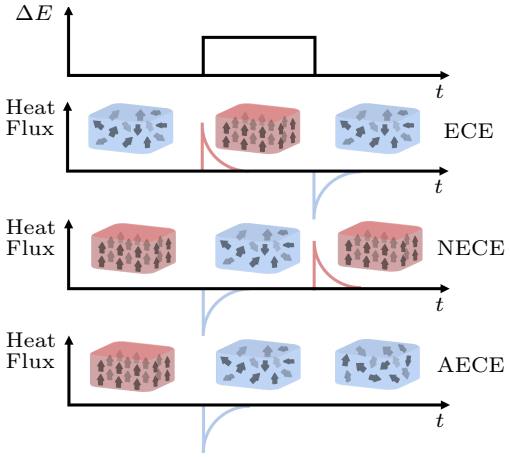


Fig. 5. Schematic illustrations of the ECE, NECE, and AECE with respective heat signals under an electric pulse.[45]

3. Electrocaloric materials

The field-responsive polarization switching observed in ferroelectrics is intrinsically linked to their EC properties. Ferroelectricity was discovered in 1920 by Valasek in Rochelle salt.[46] The ECE was first discovered in Rochelle salt by Kobeko and Kurtschatov in 1930.[11] This initial observation was later quantitatively confirmed by Wiseman and Kuebler in 1963, who detected a measurable temperature change of $\Delta T = 0.003$ °C via improved experimental techniques.[47] In 1992, Sinyavsky and Brodyansky pioneered the first EC cooling device by using $PbSc_{0.5}Ta_{0.5}O_3$ (PST) ceramic as the working material, which achieved a temperature span of 5 K under an electric field of 6 MV/m.[48] The device operated on an active electrocaloric refrigeration (AER) cycle, which was designed to amplify the limited temperature span that was caused by the modest ECE of the PST ceramics ($\Delta T = 1.3$–1.5 K under 2.5 MV/m in air). However, the performance of the device was constrained by several factors, including the material's low breakdown field strength and weak EC response. The study of the ECE experienced a resurgence in 2006 when a notable temperature change of 12 K was reported in a $PbZr_{0.95}Ti_{0.05}O_3$ thin film at $T = 226$ °C,[7] followed by the observation of a comparable ECE (~ 12 K) at $T = 55$ °C in organic P(VDF-TrFE) copolymer thin films in 2008.[8] These discoveries sparked accelerated advancements in EC materials.

EC materials are classified into three primary systems: normal ferroelectrics, relaxor ferroelectrics, and antiferroelectrics. The ECE originates from entropy change that

is induced by electric fields, particularly near phase transitions where significant variations in lattice volume and strain occur.[49] Materials that exhibit phase transitions with multiple polar states can achieve enhanced entropy changes when the polarization reaches saturation under high electric fields.[50] In ferroelectric materials, enhanced entropy changes occur during phase transitions.[9,51] The invariant critical point (ICP) enhancement method that was proposed by Liu *et al.* maximizes coexisting phases to achieve a large ECE.[50] However, conventional ferroelectrics often suffer from narrow phase transition temperature ranges, which relaxor ferroelectrics address through diffuse phase transitions, albeit with a reduced inherent ECE.[52] To achieve this goal, Li *et al.*[29] discovered giant EC materials with broad temperature ranges in relaxor ferroelectric polymer systems, including ternary ferroelectric polymers P(VDF-TrFE-CFE) and electron-irradiated P(VDF-TrFE). Unlike conventional ferroelectrics, relaxor ferroelectrics lack sharp first-order phase transitions and instead contain randomly oriented polar nanoregions (PNRs) with minimal polarization hysteresis. Over a wide temperature range, these PNRs can be effectively polarized under electric fields while maintaining high dipole entropy and disorder at zero field. The PNRs in relaxors contribute to additional entropy changes, which enhance their EC properties.[14,21] Antiferroelectrics exhibit unique behaviors, including the negative ECE near room temperature, as observed in the $(Pb_{0.97}La_{0.02})(Zr_xSn_{0.94-x}Ti_{0.06})O_3$ (PLZST) system, which demonstrates coexisting positive and negative ECEs, thus showing promise for efficient solid-state cooling.[53]

Researchers have explored various inorganic and organic insulators, including organic nanocomposites, to further enhance the overall performance of EC materials. The results that have been reported for both inorganic and organic EC materials are summarized in Tables 1 and 3. The study of inorganic ferroelectric materials has spanned more than a century and has included a vast array of material systems. Recent research on inorganic EC materials has focused on Pb-based materials such as $PbTiO_3$[20,57] and lead-free materials such as $BaTiO_3$,[28,55,73] including their single crystal forms, ceramic solid solutions, and various two-dimensional materials. Among these materials, inorganic EC materials consist primarily of ceramics and single crystals, which can be categorized by thickness into bulk materials, thick films (micrometer-scale), and thin films (nanometer-scale). L. Shebanovs *et al.*[74] proposed the use of thin-film materials to achieve giant ECE, although this idea was not fully realized at the time because of limitations in thin-film fabrication technology. A breakthrough occurred in 2006 when A. S. Mischenko *et al.*[7] indirectly measured the ECE in a 350 nm-thick $PbZr_{0.95}Ti_{0.05}O_3$ antiferroelectric thin film via Maxwell's relations. Under an electric field of 900 kV/cm near the Curie temperature of the material (220 °C), a maximum temperature change of $\Delta T = 12$ °C was observed. Table 2 demonstrates that even minor compositional adjustments within a specific perovskite oxide system can lead to significant variations in the EC performance, as indicated by the substantial changes in the $\Delta T/\Delta E$ value. For instance, in the barium zirconate titanate (BZT) system, a slight increase in the zirconium content from BZT1 ($Zr = 0.15$) to BZT ($Zr = 0.20$) alters the response from 0.35 °C·m·MV^{-1} to 0.38 °C·m·MV^{-1}, and other systems show even higher sensitivity. Similarly, in systems with multiple substituents such as BHSZT or BSHSZT, small changes in the concentrations of Hf, Sn, Zr, or Sr can cause the EC coefficient to vary dramatically, which underscores the critical importance of meticulous stoichiometric control in tailoring the performance of inorganic EC materials.

In the field of organic EC materials, research has focused mainly on PVDF-based polymer organic-inorganic nanocomposites. By carefully controlling parameters such as the nanofiller composition, geometry, and interfacial properties of these nanocomposites, superior dielectric breakdown strength, thermal conductivity, and enhanced polarization can be achieved. Zhang *et al.*[69] demonstrated remarkable performance in relaxor ferroelectric polymer composites. This breakthrough inspired subsequent discoveries of giant ECE in various PVDF-based polymers and their composites.

Table 1. ECE in inorganic materials.

Material	Form	T (K)	ΔE (MV/m)	ΔS (J/(kg·K))	ΔT (K)	Method	Ref.
BZT	ceramic	312	14.5	8	4.5	direct (heat flux sensor)	[28]
$BaZr_{0.2}Ti_{0.8}O_3$	thick film	313	9.7	8.5	4.9	direct (DSC)	[25]
BT	single crystal	412	1	1.9	1.6	direct (DSC)	[54]
BT	MLCC	353	80	10.1	7.1	direct (DSC)	[55]
Doped BT	MLCC	300	30	/	0.5	direct (thermometer)	[56]
PMN	bulk ceramic	340	9	/	2.5	direct (thermistor)	[16]
0.9PMN-0.1PT	thin film	298	10.5	/	0.23	direct (SThM)	[57]
PMN-0.35PT	thin film	413	74.7	/	31	indirect	[58]
PMN-0.07PT	thin film	298	72.3	/	9	indirect	[59]
PZT	thin film	499	48	/	12	indirect	[7]
PLZT	thin film	318	120	50	40	direct (thermistor)	[21]
$CuInP_2S_6$	thin film	315	14.2	5.8	3.3	indirect	[60]
$(Ba_{0.85}Sr_{0.15})(Sn_{0.05}Ti_{0.95})O_3$	ceramic	320	3	/	1.44	direct (thermocouple)	[61]
$(Ba_{0.8}Sr_{0.2})(Hf_{0.025}\ Sn_{0.025}\ Zr_{0.025}\ Ti_{0.925})O_3$	thick film	298	10	15	10	direct (*in-situ* calibration)	[62]

Table 2. Chemical compositions of the perovskite oxides that were studied in Ref. [62] (Reproduced with permission from Ref. [62]).

	Ba	Sr	Ca	Hf	Sn	Zr	Ti	O	$\Delta T/\Delta E$ (°C·m·MV^{-1})
BT	1	0	0	0	0	0	1	3	0.1
BZT	1	0	0	0	0	0.2	0.8	3	0.38
BZT1	1	0	0	0	0	0.15	0.85	3	0.35
BZT2	1	0	0	0	0	0.25	0.75	3	0.33
BSnT	1	0	0	0	0.11	0	0.89	3	0.32
BSnT1	1	0	0	0	0.8	0	0.9	3	0.26
BSnT2	1	0	0	0	0.14	0	0.85	3	0.24
BHT	1	0	0	0.17	0	0	0.83	3	0.3
BHT1	1	0	0	0.15	0	0	0.85	3	0.25
BHT2	1	0	0	0.2	0	0	0.8	3	0.24
BSrT	0.7	0.3	0	0	0	0	1	3	0.43
BSrT1	0.75	0.25	0	0	0	0	1	3	0.37
BSrT2	0.65	0.35	0	0	0	0	1	3	0.4
BCT	0.9	0.1	0	0	0	0	1	3	0.06
BCT1	0.85	0.15	0	0	0	0	1	3	0.04
BCT2	0.8	0.2	0	0	0	0	1	3	0.03
BSnZT	1	0	0	0	0.065	0.065	0.87	3	0.36
BSnZT1	1	0	0	0	0.015	0.15	0.835	3	0.32
BSnZT2	1	0	0	0	0.05	0.09	0.86	3	0.33
BHZT	1	0	0	0.09	0	0.09	0.82	3	0.33
BHZT1	1	0	0	0.04	0	0.16	0.8	3	0.28
BHZT2	1	0	0	0.14	0	0.04	0.82	3	0.29
BHST	1	0	0	0.07	0.07	0	0.86	3	0.32
BHST1	1	0	0	0.03	0.09	0	0.88	3	0.28
BHST2	1	0	0	0.14	0.02	0	0.84	3	0.28
BSCT	0.7	0.295	0.05	0	0	0	1	3	0.38
BSCT1	0.7	0.2	0.1	0	0	0	1	3	0.21
BSCT2	0.8	0.15	0.05	0	0	0	1	3	0.33
BSrZT	0.8	0.2	0	0	0	0.15	0.85	3	0.44
BSrZT1	0.85	0.15	0	0	0	0.2	0.8	3	0.39
BSrZT2	0.75	0.25	0	0	0	0.15	0.85	3	0.4
BSST	0.9	0.1	0	0	0.1	0	0.9	3	0.3
BSST1	0.88	0.12	0	0	0.08	0	0.92	3	0.27
BSST2	0.92	0.08	0	0	0.12	0	0.88	3	0.25
BSHT	0.75	0.25	0	0.03	0	0	0.97	3	0.28
BSHT1	0.9	0.1	0	0.1	0	0	0.9	3	0.14
BSHT2	0.95	0.05	0	0.14	0	0	0.86	3	0.19
BCZT	0.89	0	0.11	0	0	0.11	0.89	3	0.17
BCZT1	0.91	0	0.09	0	0	0.14	0.86	3	0.14
BCZT2	0.88	0	0.12	0	0	0.1	0.9	3	0.11
BHSZT	1	0	0	0.055	0.055	0.055	0.835	3	0.44
BHSZT1	1	0	0	0.05	0.05	0.07	0.83	3	0.42
BHSZT2	1	0	0	0.05	0.05	0.05	0.85	3	0.37
BHSZT3	1	0	0	0.06	0.06	0.06	0.82	3	0.27
BHSZT4	1	0	0	0.07	0.07	0.07	0.79	3	0.25
BSHSZT	0.8	0.2	0	0.025	0.025	0.025	0.925	3	0.98
BSHSZT1	0.8	0.2	0	0.02	0.02	0.02	0.94	3	0.96
BSHSZT2	0.8	0.2	0	0.03	0.03	0.03	0.91	3	0.97
BSHSZT3	0.7	0.3	0	0.02	0.02	0.02	0.94	3	0.89
BSHSZT4	0.7	0.3	0	0.03	0.03	0.03	0.91	3	0.84
BSHSZT5	0.9	0.1	0	0.04	0.04	0.04	0.88	3	0.87
BSHSZT6	0.9	0.1	0	0.05	0.05	0.05	0.85	3	0.91
BSCHSZT	0.905	0.09	0.005	0.0307	0.0307	0.0307	0.9079	3	0.85
BSCHSZT1	0.95	0.04	0.01	0.022	0.04	0.03	0.9079	3	0.57
BSCHSZT2	0.95	0.025	0.025	0.022	0.04	0.03	0.9079	3	0.48
BSCHSZT3	0.95	0.04	0.01	0.0307	0.0307	0.0307	0.9079	3	0.83
BSCHSZT4	0.95	0.025	0.025	0.0307	0.0307	0.0307	0.9079	3	0.38

A viable strategy for increasing the ECE in materials is to tune the polar entropy under zero electric field (Fig. 6(a)) and to reduce the energy barrier for dipole switching (Fig. 6(b)). The polar entropy measures the disorder within the microscopic polar structures of a system, where a strongly disordered state (Figs. 7(a) and 7(b)) that is characterized by a high density of polar

Table 3. ECE in organic materials.

Material	Form	T (K)	ΔE (MV/m)	ΔS (J/(kg·K))	ΔT (K)	Method	Ref.
P(VDF-TrFE) 55/45 mol%	polymer	353	209	62	12.6	indirect	[8]
P(VDF-TrFE) 55/45 mol%	polymer	340	120	70	12	direct (calorimeter)	[63]
P(VDF-TrFE) 68/32 mol%	polymer	306	160	95	20	direct (IR sensor)	[21]
P(VDF-TrFE) 65/35 mol%	polymer	323	180	160	35	direct (heat flux sensor)	[30]
P(VDF-TrFE-CFE) 59.2/33.6/7.2 mol%	polymer	303	150	73.5	14.8	direct (heat flux sensor)	[29]
P(VDF-TrFE-CFE) 69.7/30.3/6 mol%	polymer	313	100	60	12	direct (heat flux sensor)	[64]
P(VDF-TrFE-CFE-CTFE) 56.1/33.2/5.9/4.8 mol%	polymer	308	100	40	8	direct (heat flux sensor)	[65]
Blends(90/10)Co:65/35 mol% Ter: 59/33/8 mol%	polymer	311	100	60	12	direct (heat flux sensor)	[66]
Blends (90/10) Co: 55/45 mol% Ter: 62.5/29/8.5 mol%	polymer	300	150	50	10	direct (DSC)	[67]
P(VDF-TrFE-CFE)/PMN-PT	polymer composite	303	180	/	31	direct (heat flux sensor)	[68]
P(VDF-TrFE-CFE)/BST	polymer composite	296	150	/	23	direct (heat flux sensor)	[69]
P(VDF-TrFE-CFE)/BNNS/BST	polymer composite	313	200	/	35	direct (heat flux sensor)	[70]
P(VDF_{65}-$TrFE_{35}$-CFE_{7-x}-DB_x)	polymer	298	100	80	16	direct (*in-situ* calibration)	[15]
DMHD-modified P(VDF-TrFE-CFE)	polymer	298	100	100	20	direct (*in-situ* calibration)	[71]
Liquid crystal 5CB	fluidic	312	90	23.6	5.26	indirect	[72]

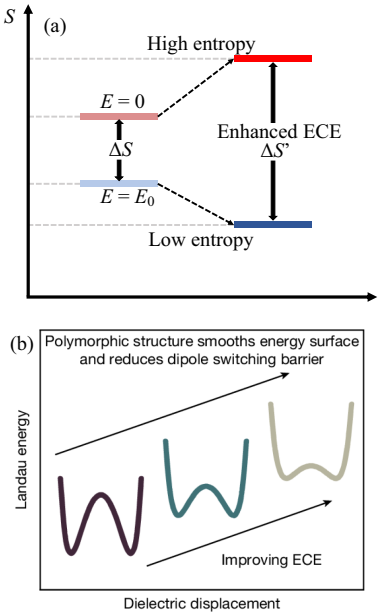


Fig. 6. (a) Approach for increasing the ECE, which includes tuning down the low-entropy state at $E = E_0$ (E_0 being the strength of the applied field) and tuning up the high-entropy state at $E = 0$, and (b) high-polar-entropy design with a flatter energy surface, which enables the coexistence of polymorphic polar states.[62] (Reproduced with permission from Ref. [62]).

entities with high orientational degeneracy signifies a system feature of high polar entropy (HPE). Recent breakthroughs in EC materials have demonstrated giant ECEs in both high-entropy polymers and perovskite oxides. Qian *et al.*[15] achieved a remarkable ECE in a high-entropy polymer through defect engineering, where a reduced CFE content and introduced double bonds (DBs) created a loosely correlated, high-entropy state with low energy barriers for field-induced switching. This defect-modified polymer exhibited a temperature change of 7.5 K under 50 MV/m, which was a 275% increase over that of conventional EC polymers. The system's exceptional performance stems from its ability to transition between a low-entropy polarized state ($E = E_0$) and a high-entropy state ($E = 0$), as shown in Fig. 6(a). The optimized TD-0.6% composition showed entropy changes that exceeded 25 $J{\cdot}kg^{-1}{\cdot}K^{-1}$ under 50–70 MV/m, which were attributed to improved crystallinity and reduced crystal size from defect modification.

Similarly, the concept of high-entropy design has been successfully applied to perovskite oxides. Du *et al.*[62] achieved a breakthrough in lead-free ferroelectric ceramics by deliberately disrupting the ordered polar structure at the atomic scale to create a novel high-entropy ceramic with a highly disordered lattice configuration. This innovative approach significantly enhanced the giant ECE in the BSH-SZT system, with an entropy change of 15 $J{\cdot}kg^{-1}{\cdot}K^{-1}$ under an electric field of 10 MV/m. The results of phase-field simulations (Figs. 7(c)–7(e)) reveal that composition inhomogeneities perturb the formation of domain structures in HPE ceramics at the atomic scale, which results in increased structural heterogeneities. These findings suggest that the introduction of composition inhomogeneities first reduces the size of polar domains. These findings for both polymeric and ceramic high-entropy systems establish defect engineering and entropy optimization as universal strategies for the development of high-performance EC materials. It is worth noting that the ECE measurements in both studies utilized the *in-situ* calibration method described in Subsection 2.2.

Beyond the strategy of introducing HPE, similar performance enhancements can be achieved by engineering interfaces at the micro-scale. Zheng *et al.*[71] used organic crystal dimethylhexynediol (DMHD) as a three-dimensional sacrificial master to assemble polar conformations at the heterogeneous interface in poly(vinylidene fluoride)-based terpolymer. Under a low electric field, the interface-augmented terpolymer had a high entropy change of 100 J/(kg·K). This interface polarization strategy is generally applicable to dielectric capacitors, supercapacitors, and other related applications.

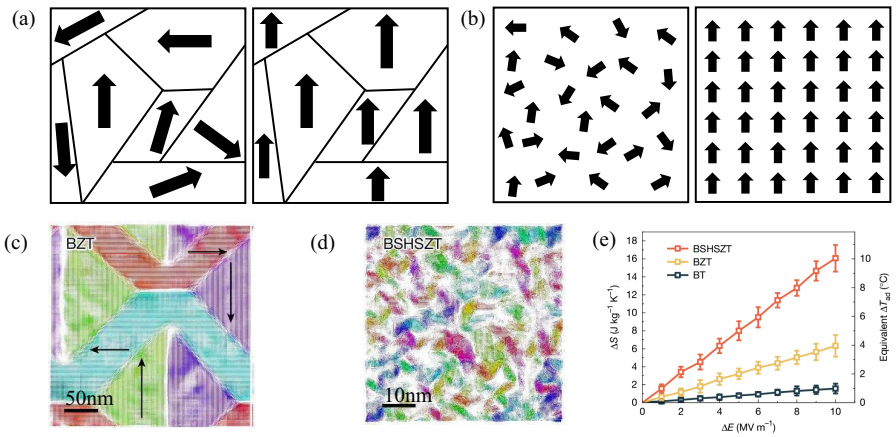


Fig. 7. Schematic illustrations of the ferroelectric dipolar state (a) without and (b) with a high-polar-entropy (HPE) configuration. Polarization configurations of (c) BZT and (d) BSHSZT under zero electric field and room-temperature conditions from phase-field simulations. (e) An entropy change of 15 J·kg^{-1}·K^{-1} under an electric field of 10 MV·m^{-1} for BSHSZT represents a substantial increase compared with those of unsubstituted BT and BZT.[62] (Reproduced with permission from Ref. [62]).

Notably, in Refs. [62,71], the field-induced ferroelectric polar structure response and the corresponding ECE were investigated by phase-field modeling. The time-dependent Ginzburg–Landau equation (Eq. (23)) was used for the temporal evolution of the domain structure that follows a minimization of the free energy of the system with respect to the polarization field. For example, in Ref. [62], the effects of multi-element substitutions at A- and B-sites were incorporated into the phase-field model by introducing spatial fluctuations into the free-energy equations. These substitutions increase the electric-field tunability of polar orders in HPE ceramics. Such enhanced tunability originates from the diverse local structural states that are generated by chemical inhomogeneity, which leads to a flattened energy landscape and promotes transitions between disordered and ordered polar states. The simulated enhancement in entropy change aligns well with the experimental calorimetry data, which further validates the effectiveness of the high-entropy strategy in the design of ferroelectric materials with superior EC performance.

In the study of ECEs in materials, researchers have employed various approaches to enhance performance, including material compositing,[70,75,76] chemical doping,[36,77] strain engineering,[78,79] and domain engineering.[80] Moreover, the discovery of novel ferroelectric systems such as 2D ferroelectrics and molecular ferroelectrics has significantly expanded the material library for ECE research. Si *et al.*[60] first reported the ECE in a van der Waals layered 2D ferroelectric material ($CuInP_2S_6$, CIPS), which achieved a high EC strength ($\Delta T/\Delta E \sim 0.292$ K·m/MV) near room temperature (315 K) under an electric field of 7.26 MV/m. A unique feature of 2D ferroelectric materials is their weak interlayer van der Waals interactions, which facilitate the formation of van der Waals heterostructures. This characteristic leads to distinct out-of-plane polarization switching behaviors that can significantly influence ferroelectric and EC properties. Li *et al.*[81] demonstrated the ECE in an organic-inorganic molecular ferroelectric ($C_3N_2H_5ClO_4$, $ImClO_4$), which exhibited a second-order FE–PE phase transition. Unlike the polarization in conventional inorganic displacement-type ferroelectrics, the polarization in $ImClO_4$ arises from the order-disorder transition of $[ClO_4]^-$ that is induced by charge transfer. Owing to their low acoustic impedance and operating voltage, FE liquid crystalline polymers show great potential for advanced EC performance.[82] These novel EC materials with outstanding performance represent a new frontier in solid-state refrigeration research and offer exciting opportunities for the future development of EC materials.

4. Mechanism of the EC refrigeration cycle and energy efficiency evaluation

While significant progress has been achieved in optimizing EC materials with enhanced isothermal entropy change and adiabatic temperature change, bridging the gap between material performance and practical cooling applications remains a critical challenge. The realization of efficient EC cooling systems depends not only on the intrinsic properties of EC materials but also on the design of thermodynamic cycles and thermal regeneration strategies. In this section, we shift our focus from material characterization to the operational principles of EC refrigeration cycles, and analyze their thermodynamic mechanisms and key performance metrics, such as the coefficient of performance (COP), temperature span and cooling power density.

The EC refrigeration cycle is a thermodynamic process that uses the reversible temperature change in a dielectric material when subjected to an electric field, and operates through a continuous sequence of polarization, heat exchange, and depolarization, similar to the vapor compression cycle, as shown in Fig. 8. The cycle begins with the adiabatic application of an electric field, which forces the dipoles in the material to align,

thereby increasing polarization. This alignment significantly reduces the polarization entropy associated with dipole disorder. Under adiabatic conditions (where no heat is exchanged with the surroundings, and thus the total entropy of the system remains constant), this decrease in polarization entropy is compensated by an increase in the thermal entropy, manifesting macroscopically as a temperature rise. The material then enters a constant-electric-field phase. While maintained under the electric field, it rejects the generated heat to the environment. This heat transfer allows the material to return to its initial temperature while remaining in a polarized state. Next, the electric field is adiabatically removed, thus enabling the dipoles to randomize again, which increases polarization entropy. To maintain constant total entropy in this adiabatic step, the corresponding energy is drawn from the internal thermal energy of the material, resulting in a macroscopic temperature drop. Finally, with no field applied, the cooled material absorbs heat from the surroundings, thereby completing the refrigeration effect. This closed-loop process is then repeated to enable continuous refrigeration or heat pumping.

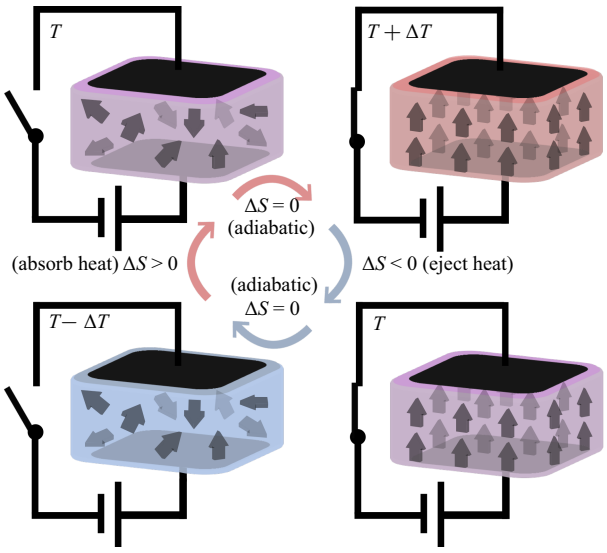


Fig. 8. Illustration of the EC refrigeration cycle.

The commonly adopted thermodynamic cycles for EC refrigeration include the Carnot cycle, Brayton cycle, and Ericsson cycle, as shown in Fig. 9. The work w that is required to transfer heat from the cold to the hot environment is represented by the area enclosed by points 1, 2, 3, and 4, whereas the cooling heat that is extracted from the cold environment corresponds to the area under the curve when the field is removed. The COP of this cycle, which quantifies the cooling effect q_c relative to the work input w, represents the ideal refrigeration limit that is achievable by such a system:

$$\mathrm{COP}_{\mathrm{Carnot}} = \frac{q_c}{w} = \frac{T_C}{T_H - T_C}. \tag{33}$$

However, a key drawback of the Carnot cycle is its reliance on four distinct electric field intensities, which complicates its practical implementation. Additionally, the achievable temperature span between the hot and cold sources is constrained by the material's adiabatic temperature change during polarization and depolarization, which limits its applicability in scenarios that require larger temperature differentials.

The ideal Brayton cycle, which is shown in Fig. 9(c), comprises two adiabatic and two isofield processes. Although it cannot reach the Carnot cycle COP, the Brayton cycle can still deliver excellent performance when EC refrigerants with parallel temperature–entropy (T–S) curves are used. A key advantage is its operational simplicity, which requires only two distinct electric field intensities in the cycle.

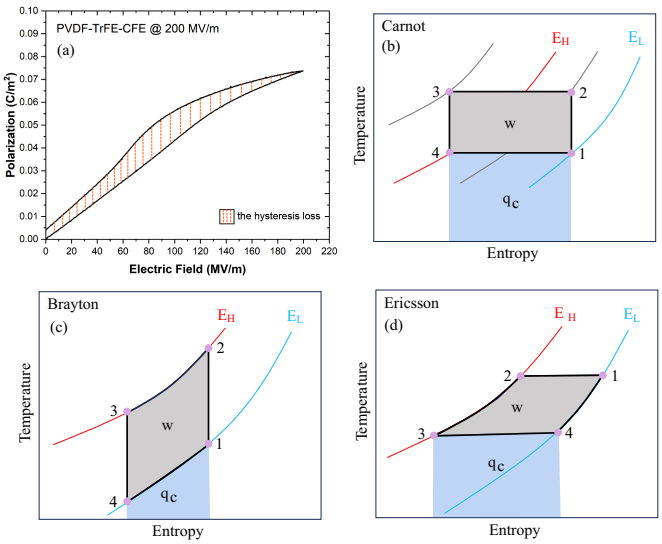


Fig. 9. (a) Polarization–electric field loop of the relaxor ferroelectric polymer P(VDF-TrFE-CFE) and schematic illustrations of electrocaloric (b) Carnot, (c) Brayton, and (d) Ericsson refrigeration cycles.

In contrast, the Ericsson cycle replaces the Brayton cycle's adiabatic processes with isothermal processes (Fig. 9(d)). However, owing to its irreversible processes, the Ericsson cycle suffers from reduced efficiency. As a result, its COP consistently remains below that of the reversible Carnot refrigeration cycle over the same temperature span.

In principle, the energy that is input to the EC material can be determined by analyzing the polarization–electric field (P–E) hysteresis loop. The ideal COP of an EC material can be evaluated according to the following equation:[10,83]

$$\mathrm{COP}_{\mathrm{Mat}} = \frac{T_C \Delta S_{\mathrm{ECE}} - \frac{1}{2} E_{\mathrm{Hyst}}}{(T_H - T_C)\Delta S_{\mathrm{ECE}} + E_{\mathrm{Hyst}}}, \tag{34}$$

where T_C and T_H denote the temperatures of the cold and hot ends, respectively; ΔS_{ECE} represents the electric-field-induced entropy change; and E_{Hyst} accounts for the hysteresis energy loss (Fig. 9(a)). The factor of 1/2 preceding E_{Hyst} in the numerator is an approximation, accounting for the portion of this hysteretic loss that is specifically attributed to the cooling half cycle. It is crucial to note that in a practical device, the total irreversible energy loss significantly exceeds the value that is

calculated solely from the *P*–*E* loop analysis due to additional losses.

The device-level COP is influenced by multiple factors beyond material properties,[84] which results in a lower value than the material COP. For EC cooling devices, the device COP can be expressed as follows:

$$\mathrm{COP}_{\mathrm{Dev}} = \frac{T_{\mathrm{C}}\Delta S_{\mathrm{ECE}} - \frac{1}{2}E_{\mathrm{Hyst}} - E_{\mathrm{HeatTrans}}}{(T_{\mathrm{H}} - T_{\mathrm{C}})\Delta S_{\mathrm{ECE}} + E_{\mathrm{Hyst}} + E_{\mathrm{FD}} + E_{\mathrm{Driver}}}, \quad (35)$$

where $E_{\mathrm{HeatTrans}}$ accounts for the heat transfer losses that arise from imperfect thermal coupling between materials and heat dissipation to the surroundings, which directly affects heat flux measurements and cooling power density; E_{FD} represents the energy that is consumed by the high-voltage generator when switching the electric field, which is quantified through leakage current tests; and E_{Driver} denotes parasitic power losses from auxiliary components such as pumps, fans, valves, and control systems.

Importantly, the selection of an appropriate thermodynamic cycle is crucial, especially because it enables improved efficiency and aids in the design of refrigeration devices.

5. Electrocaloric devices

In 1992, Sinyavsky and Brodyansky pioneered the first EC cooling device by using a PST ceramic, and measured a 5 K temperature span under an electric field of 6 MV/m.[48] The device employed an AER cycle to amplify the modest intrinsic ECE of the ceramics ($\Delta T \approx 1.3$–1.5 K at 2.5 MV/m in air). However, the performance was limited by the material's low breakdown strength, weak ECE response, and significant heat loss caused by heat exchange.

Recent advances in EC materials have spurred the development of EC device architectures, including regenerative cycles and self-regulating systems without the use of external actuators for regenerator or heat transfer fluid movement.

5.1. Regenerative EC devices

Although giant ECEs can achieve temperature changes that exceed 10 K under extreme electric fields, such temperature changes remain insufficient for practical air-conditioning applications. To address this limitation, EC cooling systems often employ AER cycles to amplify the temperature difference between the hot and cold ends. In moving-regenerator systems, the EC material cyclically shuttles between the cold and hot ends; it absorbs heat on the cold side and releases it on the hot side. The regenerator and heat transfer fluid establish a temperature gradient along the flow path, where the local temperature difference between the fluid and adjacent regenerator layers remains smaller than the system's overall temperature span. Through iterative heat exchange with the regenerator, the system accumulates cooling capacity at the cold end and dissipates heat at the hot end, thereby ultimately achieving a temperature span that exceeds the intrinsic EC temperature change. Alternatively, in stationary-material systems, the EC material remains fixed while an intermediate heat transfer fluid circulates periodically. Both approaches leverage thermal regeneration to enhance the cooling performance.

Ju *et al.*[91] proposed a device architecture that relies on giant EC materials that are actuated up and down to make alternate thermal contacts with the cold side and the heat sink side. Their model predicted that this design has the potential to achieve a cooling power density exceeding 10 W/cm^2 when operating across a 10 K temperature span. Jia *et al.*[85] later experimentally implemented and tested continuous EC cooling cycles with a T_{span} of 1 K (Fig. 10(a)). In 2013, Gu *et al.*[86] pioneered the first active regenerative EC cooling device by using polymer refrigerants. The design featured stainless steel regenerators and multilayer EC modules that were composed of 24 stacked polymer films (Fig. 10(b)). The modules executed reciprocating motion within the regenerator, which was synchronized with electric field application/removal. The system measured an impressive 6.6 K end-to-end temperature span. Plaznik *et al.*[92] developed a prototype by using PMN-10PT ceramic plates with 0.1 mm conductive silicone oil channels, which measured a 3.3 K temperature span at 50 kV/cm. A material breakthrough occurred in 2019 with PST ceramics, where multilayer capacitors demonstrated 5.5 K adiabatic temperature changes at 29 V/μm.[22] Multilayer ceramic capacitors (MLCCs) paved the way for improved AER devices: Torelló *et al.*[87] measured a span of 13 K at 15.8 MV/m in 2020 (Fig. 10(c)), and Wang *et al.*[88] measured a span of 5.2 K at 10.8 MV/m by using a laterally-moving PST MLCC (Fig. 10(d)). Li *et al.*[89] reported a fluid-pumping AER device with PST-MLC stacks (Fig. 10(e)) that measured a temperature span of 20.9 K and a cooling capacity of 2.1 W at 10 V/μm, thus indicating substantial progress toward practical applications.

Researchers have developed an AER system that employs counterrotating EC disks (Fig. 10(f)), which has been validated through both numerical simulation and experimental testing.[90,93] This design eliminates the need for separate passive regenerator layers by using the EC material layers within the counterrotating disks to serve dual functions: as both the active working medium and the regenerative heat exchange medium. Li *et al.*[94] proposed a design concept for a rotary EC device that incorporated fluid–solid conjugated heat transfer to meet the demand for highly efficient and compact cooling where the size and weight had high priority. According to their simulations, the system achieved a COP of 5.3 when operating at a temperature span of 10 K. The integrated approach significantly enhances the thermal performance of the device while simplifying its mechanical structure.

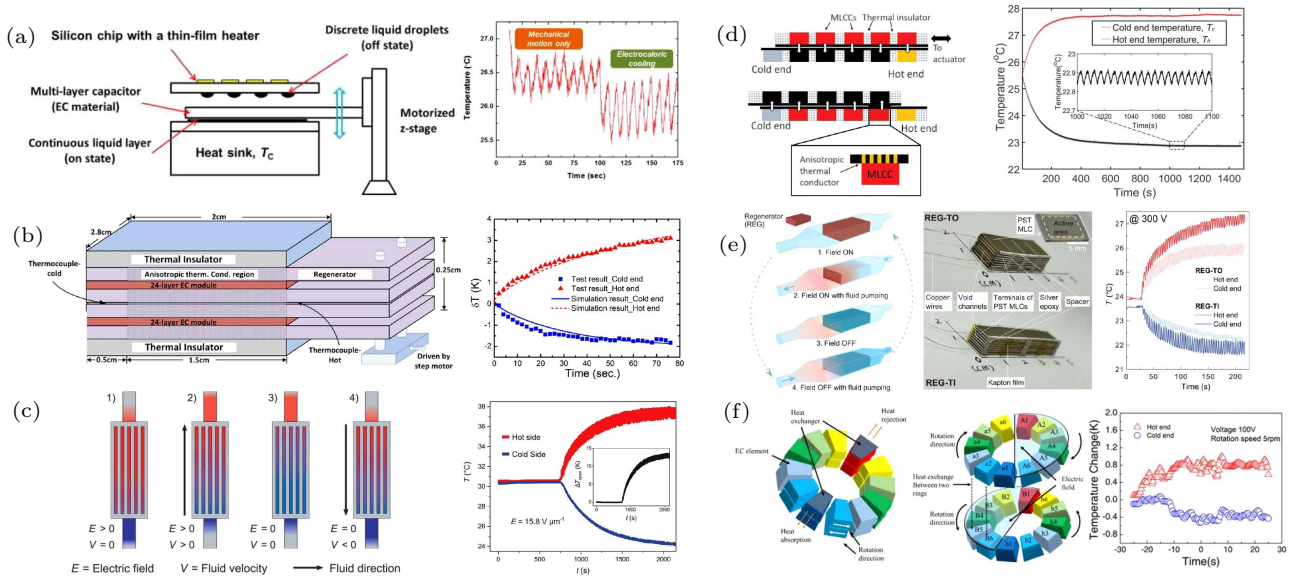


Fig. 10. Previously reported devices that are based on the EC regeneration. (Reproduced with permission from Refs. [85–90]).

5.2. Self-actuating EC devices

Current EC devices that employ AER universally require external mechanical drives to enable relative motion between the working medium and the regenerator. Consequently, such devices exhibit inherent challenges in achieving compact and lightweight EC cooling solutions. The persistent reliance on these moving-part assemblies represents a critical bottleneck in the miniaturization roadmap for EC refrigeration technology. In 2009, R. I. Epstein *et al.*[95] pioneered the application of liquid crystal thermal switches in an EC refrigeration model (Fig. 11(a)), in which the thermal conductivity variation of the liquid crystal layer effectively replaced the need for a moving heat transfer medium.

The integration of electrostrictive effects or electrostatic forces with the ECE enables the development of external-motor-free EC cooling systems, thus offering potential COP enhancement. Bradesko *et al.*[96] demonstrated this concept through simulations of a device architecture that featured actively bending EC cantilevers (Fig. 11(b)). These cantilevers exhibited significant electromechanical deformation, which enabled periodic thermal contact between adjacent elements in precise synchronization with the EC operational cycle. Building upon this electromechanical foundation, Ma *et al.*[97] developed an electrostatically-driven EC cooling device in 2017 that achieved heat transfer without the need for additional mechanical actuators (Fig. 11(c)). This design relied on flexible EC polymer films that were coupled with an electrostatic drive mechanism and measured a specific cooling power of 2.8 W/g and a COP of 13 at zero temperature span. Further advancing this method, Meng *et al.*[98] designed a cascaded EC cooling system in 2020 to increase the temperature span (Fig. 11(d)). The system integrated multiple EC polymer units with a shared electrostatic drive that operated cooperatively. By implementing a 180° phase shift between adjacent units' cooling cycles, the device enabled continuous heat transfer from the heat source to the heat sink while simultaneously promoting internal charge recycling for improved energy efficiency. Through the interconnection of four cascaded units, the system measured a maximum temperature span of 8.7 K under no-load conditions.

In 2024, Han *et al.*[99] successfully integrated EC and electrostrictive effects to create a self-driving EC refrigeration system. As shown in Fig. 11(e), this innovative design employs a 30 μm polymer film that, when activated by a single pulse, establishes self-sustaining operational cycles without the need for external mechanical drives. The device measured remarkable thermodynamic performance, with a COP that approached 24 under a 4 K temperature span. Compared to passive methods, the polymeric refrigeration system demonstrated superior cooling performance, with an immediate 17.5 K temperature reduction when applied to electronic chips. This flexible, self-regulating device integrates multiple functionalities, including thermal sensing, electromechanical actuation, and active heat pumping, to enable localized temperature control. Building upon this foundation, Wu *et al.*[100] developed a self-regenerative heat pump (SRHP) system that incorporates cascaded EC polymer film stacks (Fig. 11(f)). This device achieved a cooling temperature span of 8.8 K below ambient temperature in 30 s and delivered a maximum specific cooling power of 1.52 W/g.

Despite significant progress in the development of EC cooling devices, the absence of unified testing standards remains a major challenge. Most evaluations that are conducted under zero temperature span, although straightforward for characterizing intrinsic material properties (e.g., ΔT and ΔS), fail to reflect the real cooling performance of different types of EC devices. Such idealized measurements over-

look critical factors such as heat exchange efficiency, thermal load, and device-level energy consumption. To bridge this gap, more application-relevant approaches, such as enthalpy difference calorimetry (similar to air-conditioner rating systems),[99] which can directly assess the cooling capacity, temperature lift, and COP under practical operating conditions, should be adopted for testing. Establishing such standardized methodologies will be essential for translating material-level breakthroughs into viable EC cooling technologies.

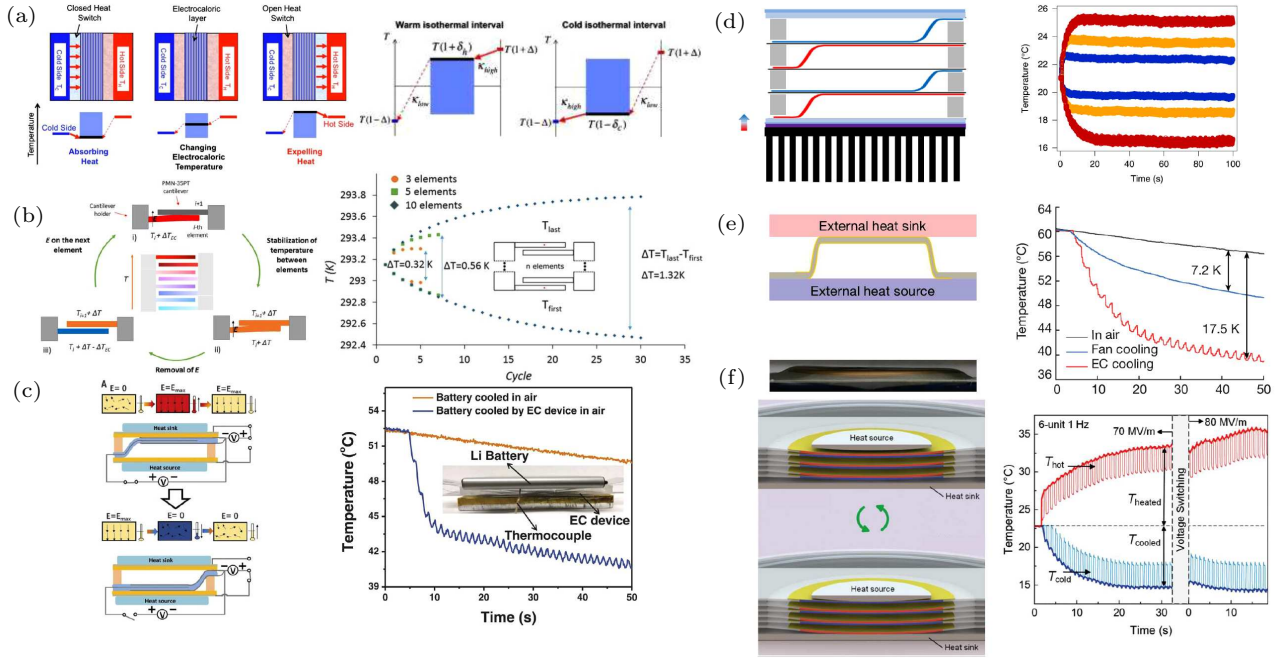


Fig. 11. Previously reported devices without external mechanical drives. (Reproduced with permission from Refs. [95–100]).

6. Summary and outlook

In this review, we provide a comprehensive overview of the ECE, from fundamental mechanisms to device applications. We begin by establishing a theoretical framework through Maxwell's relations and Landau's phenomenological theory, while also addressing the intriguing phenomenon of the NECE. We then trace the historical evolution of EC materials and compare the performance of organic and inorganic systems with particular emphasis on high-entropy material design, which opens new avenues for performance enhancement. Furthermore, we analyze the thermodynamics of ECE cooling cycles, evaluate the current state of device designs, and connect material properties to real-world engineering challenges.

With optimized EC materials exhibiting giant ECEs with minimal hysteresis and innovative thermal management strategies, researchers have successfully achieved applicable temperature spans with Watt-level cooling power densities. However, these remarkable demonstrations, which have often been achieved under idealized laboratory conditions, reveal a more pressing challenge: the transition from high-performing prototype devices to reliable, scalable, and commercially viable cooling systems. To bridge this gap, the future focus must shift from pursuing isolated material properties to developing a comprehensive design framework that prioritizes device-level performance and manufacturability.

This system-level mindset is illustrated in the comparative framework that was established by Qian *et al.*,[83] which moves beyond idealized metrics to evaluate materials under a fixed, application-relevant 10 K temperature lift. By normalizing performance against the Carnot COP, their analysis reveals a stark performance landscape: liquid–vapor refrigerants significantly dominate, whereas solid-state materials, including EC types, occupy distinct clusters on the basis of their trade-offs between normalized COP (exergetic efficiency) and nondimensional latent heat. Crucially, this methodology emphasizes that no single material excels in terms of all the metrics simultaneously. Each technology possesses a specific performance profile that is suited to particular thermal duties.

For specific material systems, specialized figures of merit (FOMs) can provide valuable guidance. Han *et al.*[76] proposed a specialized FOM for composite-based EC systems that thoughtfully incorporates factors such as entropy change, temperature change, breakdown strength, operating electric field, thermal conductivity, specific heat, filler mass ratio, and hysteresis loss ratio. Such targeted FOMs, when properly designed as mathematical combinations of the most relevant constitutive parameters, can effectively quantify performance for specific applications without over-complication.

Looking ahead, we suggest establishing an application-oriented design framework supported by a set of well-defined

device evaluation metrics. This framework should consider not only intrinsic EC properties but also critical engineering aspects such as mechanical integrity, thermal management, durability, and manufacturability. Rather than seeking a single unified FOM that attempts to encompass all performance aspects, which risks obscuring the contribution of key parameters, a more pragmatic approach would be to develop specific FOMs for different application scenarios and device architectures. This methodology will serve as a crucial guide for the rational design of next-generation EC materials and devices, accelerating the development of solid-state cooling technologies that are not only high-performing but also robust, efficient, and ready for widespread commercialization.

Beyond optimizing standalone EC cooling systems, their integration with other green refrigeration technologies presents a promising frontier for achieving superior performance and functionality. Furthermore, the convergence of EC materials with thermal metamaterials opens up revolutionary possibilities.[101] Such synergistic integration could ultimately enable intelligent thermal management solutions that are highly adaptive, efficient, and compact, pushing the boundaries of what is possible in solid-state cooling.

Acknowledgements

This work was supported by the National Key R&D Program of China (Grant Nos. 2020YFA0711500 and 2020YFA0711503), the National Natural Science Foundation of China (Grant Nos. T2488302, T2342010, and 52076127), the Natural Science Foundation of Shanghai (Grant Nos. 20ZR1471700, 22JC1401800, and 24Z511405472), the State Key Laboratory of Mechanical System and Vibration (Grant Nos. MSVZD202211, MSVZD202301, and MSVZD202401), Shanghai Jiao Tong University 2030 Initiative, Shanghai Jiao Tong University SiYuan Scholar Program, and the Student Innovation Center and the Instrumental Analysis Center at Shanghai Jiao Tong University. We acknowledge the support by Shanghai Jiao Tong University 2030 Initiative.

References

[1] Russ B, Glaudell A, Urban J J, Chabinyc M L and Segalman R A 2016 *Nature Reviews Materials* **1** 16050
[2] Franco V, Blázquez J S, Ipus J J, Law J Y, Moreno-Ramírez L M and Conde A 2018 *Progress in Materials Science* **93** 112
[3] Xu S S, Fu Q, Zhou Y F, Peng L, Gao X Q, Li Z X, Gong M Q, Dong X Q and Shen J 2023 *Chin. Phys. B* **32** 027502
[4] Xu C, Jiang X, Zou Z, Xie Z, Zhang W and Feng M 2024 *Chin. Phys. B* **33** 127501
[5] Tušek J, Engelbrecht K, Eriksen D, Dall'Olio S, Tušek J and Pryds N 2016 *Nature Energy* **1** 16134
[6] Li B, Kawakita Y, Ohira-Kawamura S, *et al*. 2019 *Nature* **567** 506
[7] Mischenko A S, Zhang Q, Scott J F, Whatmore R W and Mathur N D 2006 *Science* **311** 1270
[8] Neese B, Chu B, Lu S G, Wang Y, Furman E and Zhang Q M 2008 *Science* **321** 821
[9] Moya X, Kar-Narayan S and Mathur N D 2014 *Nat. Mater.* **13** 439
[10] Shi J, Han D, Li Z, Yang L, Lu S G, Zhong Z, Chen J, Zhang Q M and Qian X 2019 *Joule* **3** 1200
[11] Kobeko P and Kurtschatov J 1930 *Zeitschrift für Physik* **66** 192
[12] Qian X, Chen X, Zhu L and Zhang Q M 2023 *Science* **380** eadg0902
[13] Chen X, Shvartsman V V, Lupascu D C and Zhang Q M 2022 *J. Appl. Phys.* **132** 240901
[14] Pirc R, Kutnjak Z, Blinc R and Zhang Q M 2011 *Appl. Phys. Lett.* **98** 021909
[15] Qian X, Han D, Zheng L, Chen J, Tyagi M, Li Q, Du F, Zheng S, Huang X, Zhang S, Shi J, Huang H, Shi X, Chen J, Qin H, Bernholc J, Chen X, Chen L Q, Hong L and Zhang Q M 2021 *Nature* **600** 664
[16] Rožič B, Kosec M, Uršič H, Holc J, Malič B, Zhang Q M, Blinc R, Pirc R and Kutnjak Z 2011 *J. Appl. Phys.* **110** 064118
[17] Li X, Lu S G, Chen X Z, Gu H, Qian X S and Zhang Q M 2013 *J. Mater. Chem. C* **1** 23
[18] Thacher P D 1968 *J. Appl. Phys.* **39** 1996
[19] Lu S G, Rožič B, Zhang Q M, Kutnjak Z, Pirc R, Lin M, Li X and Gorny L 2010 *Appl. Phys. Lett.* **97** 202901
[20] Usui T, Hirose S, Ando A, Crossley S, Nair B, Moya X and Mathur N D 2017 *J. Phys. D: Appl. Phys.* **50** 424002
[21] Lu S G, Rožič B, Zhang Q M, Kutnjak Z, Li X, Furman E, Gorny L J, Lin M, Malič B, Kosec M, Blinc R and Pirc R 2010 *Appl. Phys. Lett.* **97** 162904
[22] Nair B, Usui T, Crossley S, Kurdi S, Guzmán-Verri G G, Moya X, Hirose S and Mathur N D 2019 *Nature* **575** 468
[23] Shan D, Pan K, Liu Y and Li J 2020 *Nano Energy* **67** 104203
[24] Bai Y, Zheng G and Shi S 2010 *Appl. Phys. Lett.* **96** 192902
[25] Ye H J, Qian X S, Jeong D Y, Zhang S, Zhou Y, Shao W Z, Zhen L and Zhang Q M 2014 *Appl. Phys. Lett.* **105** 152908
[26] Sanlialp M, Shvartsman V V, Acosta M, Dkhil B and Lupascu D C 2015 *Appl. Phys. Lett.* **106** 062901
[27] Hou Y, Yang L, Qian X, Zhang T and Zhang Q M 2016 *Phil. Tran. Roy. Soc. A: Math. Phys. Eng. Sci.* **374** 20160055
[28] Qian X S, Ye H J, Zhang Y T, Gu H, Li X, Randall C A and Zhang Q M 2014 *Advanced Functional Materials* **24** 1300
[29] Li X, Qian X S, Lu S G, Cheng J, Fang Z and Zhang Q M 2011 *Appl. Phys. Lett.* **99** 052907
[30] Li X, Qian X S, Gu H, Chen X, Lu S G, Lin M, Bateman F and Zhang Q M 2012 *Appl. Phys. Lett.* **101** 132903
[31] Qian J, Hu P, Liu C, Jiang J, Dan Z, Ma J, Lin Y, Nan C W and Shen Y 2018 *Science Bulletin* **63** 356
[32] Liu Y, Scott J F and Dkhil B 2016 *Appl. Phys. Rev.* **3** 031102
[33] Yang T, Wang B, Hu J M and Chen L Q 2020 *Phys. Rev. Lett.* **124** 107601
[34] Chen L Q 2008 *Journal of the American Ceramic Society* **91** 1835
[35] Bai Y, Zheng G P and Shi S Q 2011 *Materials Research Bulletin* **46** 1866
[36] Geng W, Liu Y, Meng X, Bellaiche L, Scott J F, Dkhil B and Jiang A 2015 *Adv. Mater.* **27** 3165
[37] Ma Y B, Grünebohm A, Meyer K C, Albe K and Xu B X 2016 *Phys. Rev. B* **94** 094113
[38] Weyland F, Bradeško A, Ma Y B, Koruza J, Xu B X, Albe K, Rojac T and Novak N 2018 *Energy Technology* **6** 1519
[39] Zhang T, Li W, Hou Y, Yu Y, Cao W, Feng Y and Fei W 2016 *RSC Advances* **6** 71934
[40] Wu H H, Zhu J and Zhang T Y 2015 *Nano Energy* **16** 419
[41] Park M H, Kim H J, Kim Y J, Moon T, Kim K D, Lee Y H, Hyun S D and Hwang C S 2016 *Adv. Mater.* **28** 7956
[42] Zhuo F, Li Q, Gao J, Wang Y, Yan Q, Zhang Y, Xi X, Chu X and Cao W 2016 *Appl. Phys. Lett.* **108** 082904
[43] Hao X, Zhai J, Kong L B and Xu Z 2014 *Progress in Materials Science* **63** 1
[44] Grünebohm A, Ma Y B, Marathe M, Xu B X, Albe K, Kalcher C, Meyer K C, Shvartsman V V, Lupascu D C and Ederer C 2018 *Energy Technology* **6** 1491
[45] Qian X, Yang T, Zhang T, Chen L Q and Zhang Q M 2016 *Appl. Phys. Lett.* **108** 142902
[46] Valasek J 1921 *Phys. Rev.* **17** 475
[47] Wiseman G G and Kuebler J K 1963 *Phys. Rev.* **131** 2023
[48] Sinyavsky Y V and and Brodyansky V M 1992 *Ferroelectrics* **131** 321
[49] Crossley S, McGinnigle J R, Kar-Narayan S and Mathur N D 2014 *Appl. Phys. Lett.* **104** 082909
[50] Liu Z K, Li X and Zhang Q M 2012 *Appl. Phys. Lett.* **101** 082904

[51] Zhao L, Ke X, Zhou Z, Liao X, Li J, Wang Y, Wu M, Li T, Bai Y and Ren X 2019 *J. Mater. Chem. C* **7** 1353
[52] Zhao C, Yang J, Huang Y, Hao X and Wu J 2019 *J. Mater. Chem. A* **7** 25526
[53] Zhuo F, Li Q, Gao J, Ji Y, Yan Q, Zhang Y, Wu H H, Xi X Q, Chu X and Cao W 2018 *ACS Applied Materials & Interfaces* **10** 11747
[54] Bai Y, Ding K, Zheng G P, Shi S Q and Qiao L 2012 *Physica Status Solidi (a)* **209** 941
[55] Bai Y, Zheng G P, Ding K, Qiao L, Shi S Q and Guo D 2011 *J. Appl. Phys.* **110** 094103
[56] Kar-Narayan S and Mathur N D 2010 *J. Phys. D: Appl. Phys.* **43** 032002
[57] Crossley S, Usui T, Nair B, Kar-Narayan S, Moya X, Hirose S, Ando A and Mathur N D 2016 *Appl. Phys. Lett.* **108** 032902
[58] Saranya D, Chaudhuri A R, Parui J and Krupanidhi S B 2009 *Bulletin of Materials Science* **32** 259
[59] Correia T M, Young J S, Whatmore R W, Scott J F, Mathur N D and Zhang Q 2009 *Appl. Phys. Lett.* **95** 182904
[60] Si M, Saha A K, Liao P Y, Gao S, Neumayer S M, Jian J, Qin J, Balke Wisinger N, Wang H, Maksymovych P, Wu W, Gupta S K and Ye P D 2019 *ACS Nano* **13** 8760
[61] Lu S G, Lin X, Li J, Li D, Yao Y, Tao T and Liang B 2021 *J. Alloys Compd.* **871** 159519
[62] Du F, Yang T, Hao H, *et al*. 2025 *Nature* **640** 924
[63] Lu S G, Rožič B, Zhang Q M, Kutnjak Z and Neese B 2011 *Appl. Phys. Lett.* **98** 122906
[64] Lu B, Chen X, Zhang T, Lu S G and Zhang Q M 2018 *Appl. Phys. Lett.* **113** 153903
[65] Chen X, Xu W, Lu B, Zhang T, Wang Q and Zhang Q M 2018 *Appl. Phys. Lett.* **113** 113902
[66] Qian X, Ye H J, Yang T, Shao W Z, Zhen L, Furman E, Chen L Q and Zhang Q 2015 *Advanced Functional Materials* **25** 5134
[67] Chen X Z, Li X, Qian X S, Wu S, Lu S G, Gu H M, Lin M, Shen Q D and Zhang Q M 2013 *Polymer* **54** 2373
[68] Li Q, Zhang G, Zhang X, Jiang S, Zeng Y and Wang Q 2015 *Adv. Mater.* **27** 2236
[69] Zhang G, Zhang X, Yang T, Li Q, Chen L Q, Jiang S and Wang Q 2015 *ACS Nano* **9** 7164
[70] Zhang G, Fan B, Zhao P, Hu Z, Liu Y, Liu F, Jiang S, Zhang S, Li H and Wang Q 2018 *ACS Applied Energy Materials* **1** 1344
[71] Zheng S, Du F, Zheng L, Han D, Li Q, Shi J, Chen J, Shi X, Huang H, Luo Y, Yang Y, O'Reilly P, Wei L, de Souza N, Hong L and Qian X 2023 *Science* **382** 1020
[72] Qian X S, Lu S G, Li X, Gu H, Chien L C and Zhang Q 2013 *Advanced Functional Materials* **23** 2894
[73] Moya X, Stern-Taulats E, Crossley S, González-Alonso D, Kar-Narayan S, Planes A, Mañosa L and Mathur N D 2013 *Adv. Mater.* **25** 1360
[74] Shebanovs L, Borman K, Lawless W N and and Kalvane A 2002 *Ferroelectrics* **273** 137
[75] Qian J, Peng R, Shen Z, Jiang J, Xue F, Yang T, Chen L and Shen Y 2019 *Adv. Mater.* **31** 1801949
[76] Han D, Du F, Zhang Y, Zheng L, Chen J, Huang X, Li Q, Zheng S, Shi J, Chen J, Dong J and Qian X 2023 *Joule* **7** 2174
[77] Yang Y, Zhou Z, Ke X, Wang Y, Su X, Li J, Bai Y and Ren X 2020 *Scripta Materialia* **174** 44
[78] Sun X, Huang H, Wang J, Wen Y and Dang Z M 2019 *J. Alloys Compd.* **777** 821
[79] Hou X, Wu H, Li H, Chen H and Wang J 2018 *J. Phys.: Condens. Matter* **30** 465401
[80] Hou X, Li H, Shimada T, Kitamura T and Wang J 2018 *J. Appl. Phys.* **123** 124103
[81] Li W, Jafri H M, Zhang C, Zhang Y, Zhang H, Huang H, Jiang S and Zhang G 2020 *J. Mater. Chem. A* **8** 16189
[82] Huang J, Kwok M H, Zhao B and Zhu L 2024 *Giant* **18** 100257
[83] Qian S, Nasuta D, Rhoads A, Wang Y, Geng Y, Hwang Y, Radermacher R and Takeuchi I 2016 *International Journal of Refrigeration* **62** 177
[84] Hou H, Qian S and Takeuchi I 2022 *Nature Reviews Materials* **7** 633
[85] Jia Y and Sungtaek Ju Y 2012 *Appl. Phys. Lett.* **100** 242901
[86] Gu H, Qian X, Li X, Craven B, Zhu W, Cheng A, Yao S C and Zhang Q M 2013 *Appl. Phys. Lett.* **102** 122904
[87] Torelló A, Lheritier P, Usui T, Nouchokgwe Y, Gérard M, Bouton O, Hirose S and Defay E 2020 *Science* **370** 125
[88] Wang Y, Zhang Z, Usui T, Benedict M, Hirose S, Lee J, Kalb J and Schwartz D 2020 *Science* **370** 129
[89] Li J, Torelló A, Kovacova V, Prah U, Aravindhan A, Granzow T, Usui T, Hirose S and Defay E 2023 *Science* **382** 801
[90] Zhang T, Qian X S, Gu H, Hou Y and Zhang Q M 2017 *Appl. Phys. Lett.* **110** 243503
[91] Ju Y S 2010 *Journal of Electronic Packaging* **132** 041004
[92] Plaznik U, Kitanovski A, Rožič B, Malič B, Uršič H, Drnovšek S, Cilenšek J, Vrabelj M, Poredoš A and Kutnjak Z 2015 *Appl. Phys. Lett.* **106** 043903
[93] Gu H M, Qian X S, Ye H J and Zhang Q M 2014 *Appl. Phys. Lett.* **105** 162905
[94] Li Q, Wei L, Zhong N, Shi X, Han D, Zheng S, Du F, Shi J, Chen J, Huang H, Duan C and Qian X 2024 *Nat. Commun.* **15** 702
[95] Epstein R I and Malloy K J 2009 *J. Appl. Phys.* **106** 064509
[96] Bradeško A, Juričić Đ, Santo Zarnik M, Malič B, Kutnjak Z and Rojac T 2016 *Appl. Phys. Lett.* **109** 143508
[97] Ma R, Zhang Z, Tong K, Huber D, Kornbluh R, Ju Y S and Pei Q 2017 *Science* **357** 1130
[98] Meng Y, Zhang Z, Wu H, Wu R, Wu J, Wang H and Pei Q 2020 *Nature Energy* **5** 996
[99] Han D, Zhang Y, Huang C, Zheng S, Wu D, Li Q, Du F, Duan H, Chen W, Shi J, Chen J, Liu G, Chen X and Qian X 2024 *Nature* **629** 1041
[100] Wu H, Zhu Y, Yan W, Zhang S, Budiman W, Liu K, Wu J, Meng Y, Zhao X, Mehta A, Kaur S and Pei Q 2024 *Science* **386** 546
[101] Xu H and Huang J 2025 *Chin. Phys. B* **34** 67702